Journal of Power Sources 196 (2011) 399–404

Contents lists available at ScienceDirect

Journal of Power Sources

journal homepage: www.elsevier.com/locate/jpowsour

Electrochemical evaluation of nanocrystalline Zn-doped tin oxides as anodes for lithium ion microbatteries

Morteza Torabi, S.K. Sadrnezhaad*

Materials and Energy Research Center, P.O. Box 14155-4777, Tehran, Iran

ARTICLE INFO

Article history:
Received 17 October 2009
Received in revised form 5 June 2010
Accepted 11 June 2010
Available online 22 June 2010

Keywords:
Thin-film anode
Microbattery
Lithium ion battery
Zn-doped tin oxide
Nanocrystalline

ABSTRACT

Nanocrystalline tin oxides were synthesized using electron beam evaporation (e-beam) and further heat treatment. X-ray diffraction (XRD) revealed that as-deposited samples were amorphous SnO. Heat treatment of the as-deposited thin films at 250 °C for 2 h and 500 °C for 10 h led to the formation of romarchite SnO and tetragonal SnO_2, respectively. Scanning electron microscopy (SEM) showed a compact morphology of the coatings. Elemental mapping of the films also represented homogeneous distribution of the zinc atoms in the SnO_2 structure. Atomic force microscopy (AFM) images demonstrated a fine and smooth surface of the e-beam evaporated films for the SnO samples, and rough topography for the SnO_2. Doping led to the formation of finer and more uniform surface morphology. Anodic behavior of the thin film during charge/discharge process showed that specific capacity of the pure SnO_2 increased from 502 to 903 $\mu Ah\,cm^{-2}\,\mu m^{-1}$ for nanocrystalline Zn-doped SnO_2. Moreover, specific capacity of the doped film enhanced to 137.6 that is, higher than 69.5 $\mu Ah\,cm^{-2}\,\mu m^{-1}$ for the pure SnO_2. XRD results also show that Zn doping decreased Sn clustering during cycling.

1. Introduction

Rechargeable thin-film lithium ion batteries served much attention recently due to their applications in microelectronics such as smart cards, medical devices and integrated circuits [1,2]. A thin-film microbattery is made up of a cathode, a solid electrolyte and an anode. Lithium metal was used as anode in rechargeable lithium ion batteries. Lithium metal has low melting point and is reactive to the air and water that make lithium inappropriate for integration with micro-devices. Therefore, replacing the lithium anode with other stable thin-film materials would be welcome. Many alloys and composites, such as Ni–Sn, Cu–Sn, Si–Sn, N–Sn, Zr–Sn, Sn–Zr–Ag [3–6] or metal oxides such as SnO_2 [7] were introduced and tested as anodes for Li-ion microbatteries.

Tin oxide based materials have been proposed as alternative anode materials for lithium ion batteries due to their high energy densities and stable capacity retention [8–10]. Because of formation of Li_2O in the first cyclic loading, SnO_2-based materials have displayed unusual electrochemical behavior. Li_2O formation and capacity fading caused by volume changing would be controlled using nanotechnology or doping process [11–13]. Therefore, nanocrstalline Zn-doped SnO_2 can also be suggested as a promising anode material. The particle size of the nanocrystalline Zn-doped SnO_2 is small enough to increase the active surface of the particles and materials efficiency. Furthermore, it would excel the kinetic of the lithium intercalation/deintercalation process in the lithium ion batteries [14].

In this study, synthesis of the Zn-doped SnO_2 using electron beam evaporation was investigated. Nanocrystalline Zn-doped SnO_2 was evaluated electrochemically as possible anode materials for Li-ion thin-film batteries.

2. Experimental

Nanocrystalline Zn-doped tin oxides were prepared using e-beam evaporation method. During this process, copper thin layer was firstly deposited with thickness of about 50 nm onto a 1 cm × 1 cm glass. Zn-doped tin oxides source was prepared by cold pressing (10MPa) of SnO_2 and 1 wt% ZnO powders (Merck, Germany). Prior to each deposition, vacuum was applied in the chamber until the pressure equal to 10^{-5} Pa. Then, pre-evaporating has systematically been achieved in order to clean the source surface. Two different heat treatments were applied to the as-deposited thin films. In the first, thin layers were put into the crucible in the air for 2 h at 250 °C. In the other heat treatment, the as-deposited samples were oxidized for 10 h at 500 °C.

The morphology of the Zn-doped tin oxide thin films were studied using scanning electron microscopy (SEM, VEGA, TESCAN) equipped with energy dispersive X-ray (EDX) analysis which was used for compositional analysis of the nanocrystalline Zn-doped

* Corresponding author. Tel.: +98 261 6210009; fax: +98 261 6201888.
E-mail address: sadrnezh@sharif.edu (S.K. Sadrnezhaad).

0378-7753/$ – see front matter © 2010 Elsevier B.V. All rights reserved.
doi:10.1016/j.jpowsour.2010.06.028

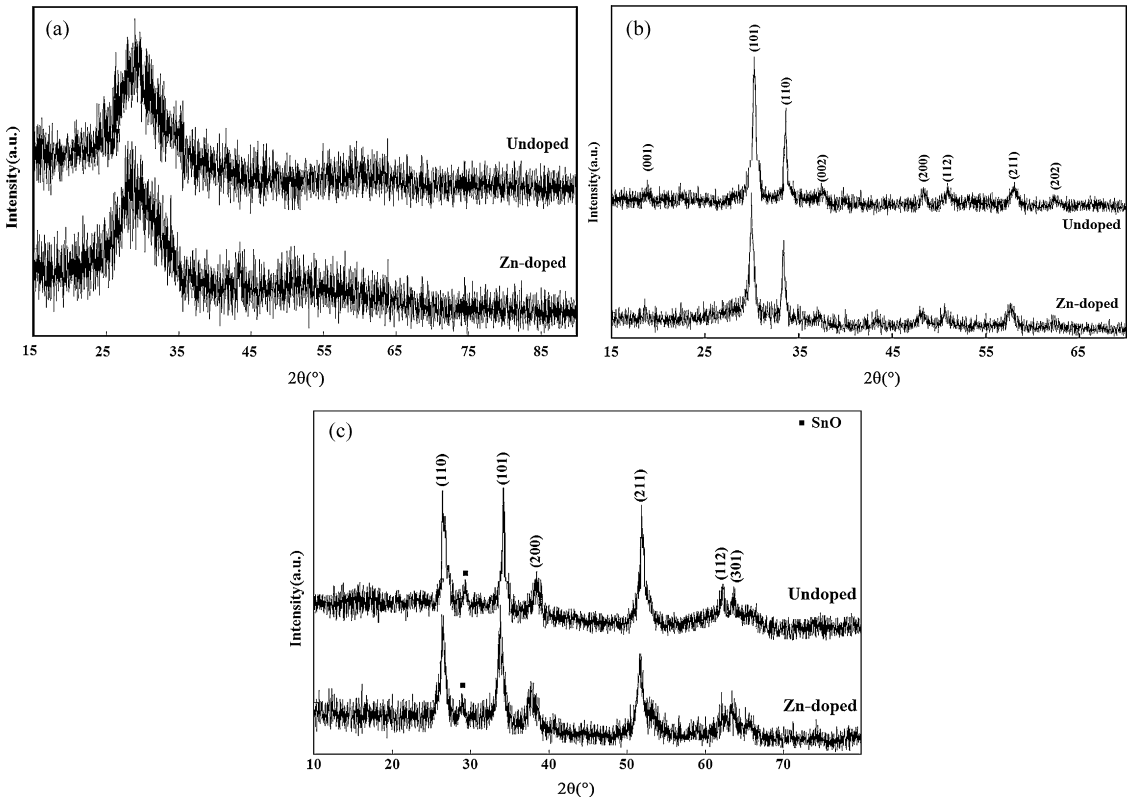

Fig. 1. X-ray diffraction of (a) as-deposited thin film, (b) heat treated at 250 °C for 2 h and (c) heat treated at 500 °C for 10 h.

tin oxides. The structural characterization of evaporated thin films was carried out by analyzing the X-ray diffraction patterns (XRD), obtained using a Unisuntis (XMD 300) diffractometer (λ = 1.5405 Å for Cu Kα radiation).

Topographic images of the deposits were also obtained by atomic force microscopy (AFM). These experiments were carried out in the ambient condition using Autoprobe CP (Parkscientific Instrument, USA).

The electrochemical measurements were performed in a Teflon homemade coin cells with lithium counter electrode and 1 M $LiBF_4$ (Aldrich, USA), ethylene carbonate (EC)/diethyl carbonate (DEC) (1:1 by volume, Merck, Germany). The cells were cycled galvanostatically at 10 $\mu A\,cm^{-2}$ in the potential range from 0 to 1.7 V.

3. Results and discussion

X-ray diffraction was used to investigate the thin-film structures that are formed during e-beam evaporation. X-ray diffraction pattern of the undoped and Zn-doped tin oxides are presented in Fig. 1.

The broad and weak peak in Fig. 1(a) indicates that the as-deposited thin films are nanocrystalline or even amorphous. A broad peak at about 30° and low conductivity of the thin film directed us to romarchite SnO (JCPDS 06-0395).

Fig. 1(b) shows XRD pattern of the heat-treated films at 250 °C for 2 h. As it is observed, well-crystallized romarchite SnO was formed during this process and confirms our first assumption about formation of the SnO during e-beam evaporation. It can be seen that the as-deposited SnO was amorphous. However, a broad peak at about 30° in Fig. 1(a) shows preferentially growth of the SnO.

Fig. 1(c) represents XRD pattern of the heat-treated samples at 500 °C for 10 h. SnO_2 was formed completely in this process. All reflections of SnO_2 are in accordance with a tetragonal rutile structure (JCPDS 41-1445). In addition, some untreated SnO were detected in the XRD pattern.

The average crystallite size of SnO and SnO_2 thin films were calculated about 21.8 nm, 27.6 nm according to XRD-Scherrer formula (Eq. (1)):

$$d = \frac{k\lambda}{B\cos\theta} \tag{1}$$

where d is the mean crystallite size, k a constant usually equal to ~0.9, λ the wavelength of Cu Kα (i.e. λ = 1.5405 Å), B the full width at half maximum intensity of the peak (FWHM) in radian and θ is Bragg's diffraction angle [15]. Such fine crystallites lead to broad and weak peaks in the XRD pattern.

The Zn doping does not affect the lattice structure of SnO_2 because of its low concentration. The diffraction peaks intensities are decreased for doped SnO_2, indicating smaller crystallite size. According to Eq. (1), the average crystallite sizes of undoped SnO and SnO_2 were about 35.4 and 46.8 nm, respectively. Moreover, the XRD spectrum of the doped thin film exhibits a leftward shift in the axis of 2θ with respect to the undoped SnO_2, due to the increment of the lattice volume of the Zn-doped SnO_2 which is attributed to the substitution of the larger Zn^{2+} ions (0.74 Å) into the Sn^{4+} (0.69 Å) sites.

Fig. 2 shows SEM images of pure and Zn-doped thin films. The thin-film surface of the as-deposited pure SnO_2 (Fig. 2(a)) represents a uniform and dense layer without any cracks and porosities. Some blisters are seen on the surface, which is a common feature of thin films deposited by e-beam evaporation. The elemental mapping was used in order to investigate the distribution of tin, especially for blisters. The results of tin map and backscatter electrons (BSE) image of undoped film show a uniform distribution of the tin on the surface and no obvious differences were observed in blisters regions. Therefore, deposition and growth are completely homogeneous.

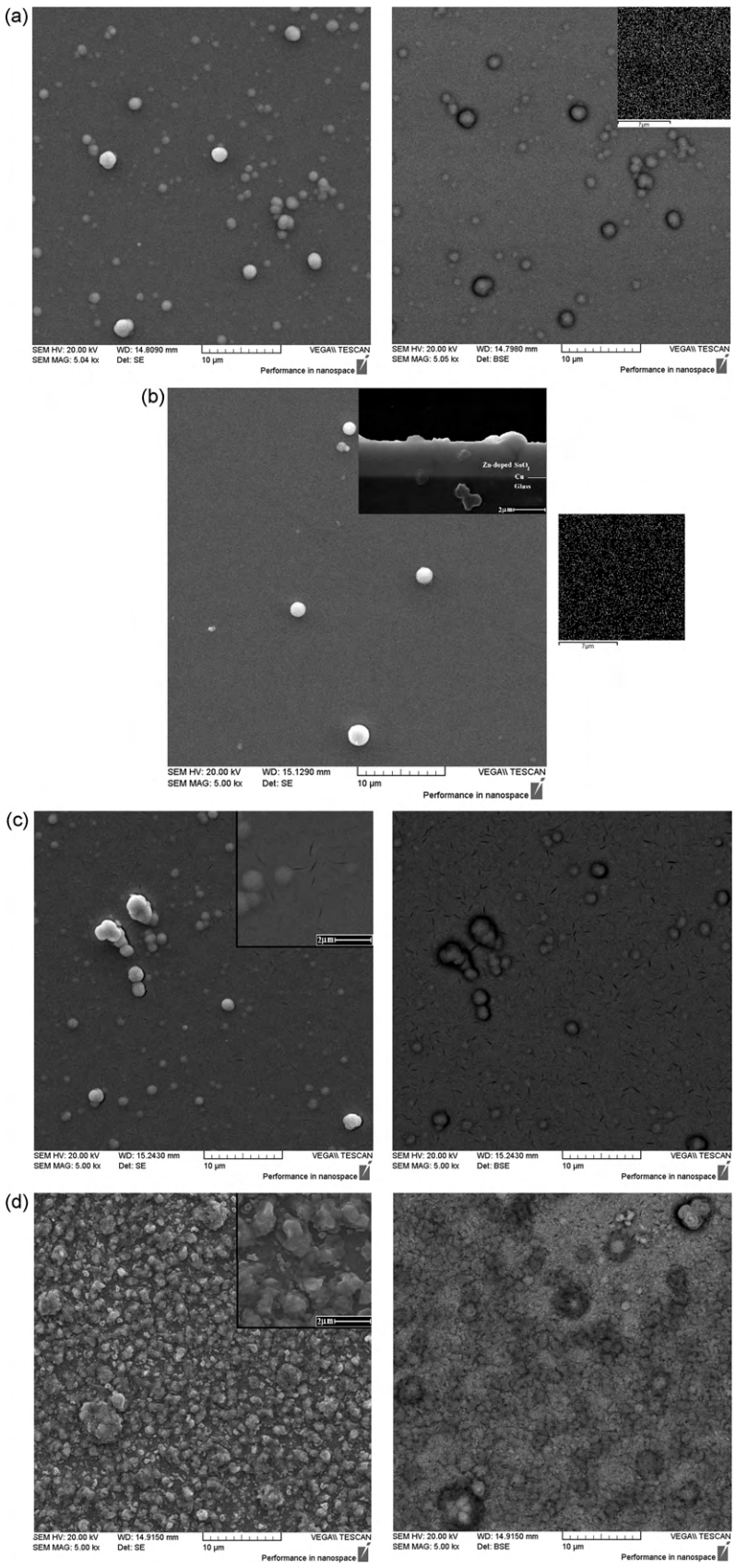

Fig. 2. (a) SEM image, BSE and Sn map of as-deposited undoped layers; (b) SEM image and Zn map of as-deposited, (c) SEM and BSE images of annealed at 250 °C for 2 h and (d) SEM and BSE images of annealed at 500 °C for 10 h of Zn-doped thin films.

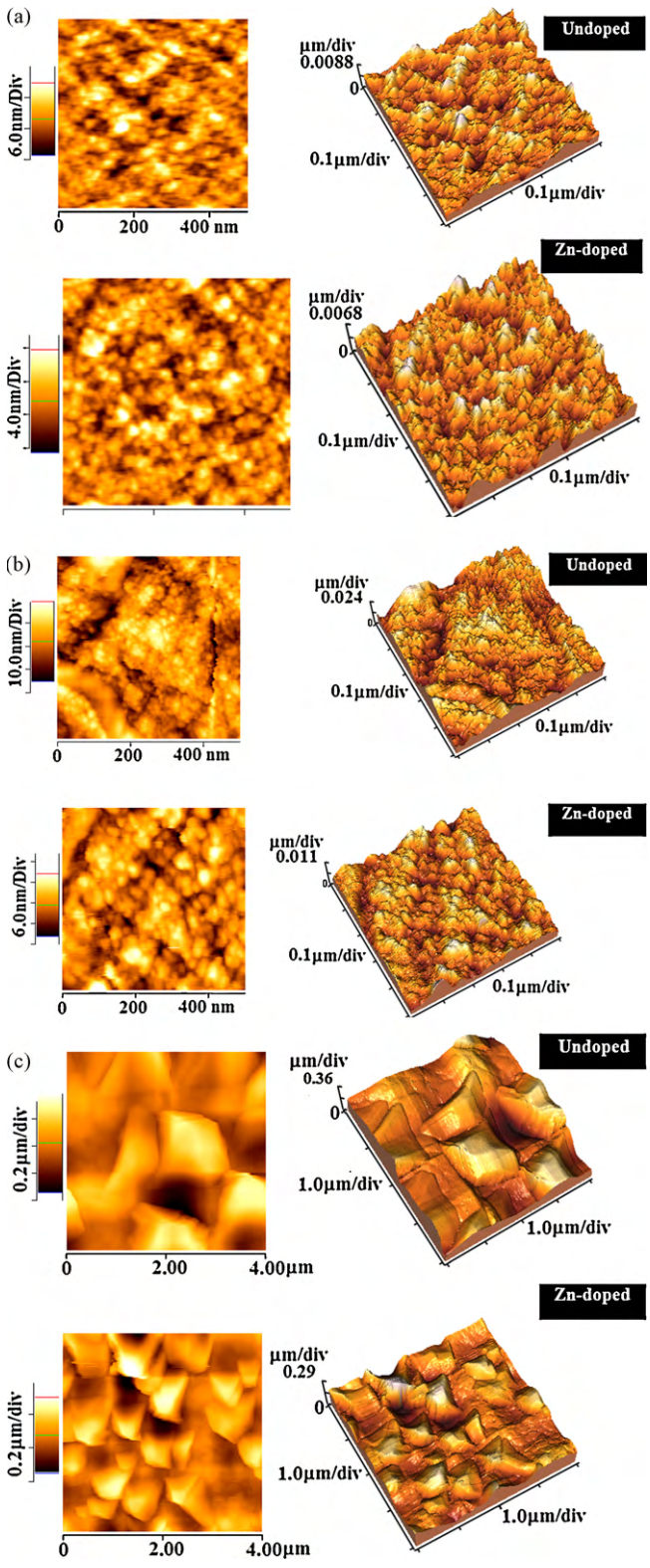

Fig. 3. AFM images of nanocrystalline undoped and Zn-doped tin oxide thin films: (a) as-deposited, (b) heat treated at 250 °C for 2 h (SnO), (c) heat treated at 500 °C for 10 h (SnO_2).

Fig. 2(b) represents the surface morphology and Zn map of as-deposited Zn-doped thin layer. The cross section of this sample (inset of the Fig. 2(b)) also shows a compact layer with thickness of about 2 µm. This map illustrates the uniform dopant solid solution observed in compositions of $Sn_{0.99}Zn_{0.01}O$. Some cracks are observed in the case of annealed thin film at 250 °C for 2 h (Fig. 2(c)). Moreover, BSE image of the thin layer illustrates a homogeneous deposit. The oxygen count in the EDS spectrum was increased in respect of the as-deposited thin layers. The blisters were also increased on the surface and made a rougher surface than the as-deposited samples.

Annealing the thin films at higher temperature (500 °C for 10 h) leads to a different morphology as it can be seen in Fig. 2(d). XRD pattern shows SnO_2 formation during this process. The surface consists of polygonal deposits that were formed and grown during heat treatment; however, the crystallite size remained unchanged. The BSE image also shows a uniform composition and crystallographic structure of the Zn-doped SnO_2 film.

AFM was used to investigate the topography of the thin films. Fig. 3 shows AFM images of undoped and Zn-doped tin oxide thin films. Fig. 3(a) represents the surface of the as-deposited tin oxides. The film that is formed by e-beam evaporation consists of regions with a very fine, spherical and uniform structure. The size of the particles varied between less than 10–25 nm for Zn-doped and 15–30 nm for undoped tin oxides. The root-mean-square (rms) roughness and *P–V* values of the doped film are 2.0 and 13.5 nm respectively that are comparable with undoped film (2.1 and 17.8 nm). It reveals finer topography of the Zn-doped films. Heat treatment has affected surface topography and roughness of the films (Fig. 3(b) and (c)). As it is revealed from XRD patterns and SEM images, annealing the as-deposited tin films leads to a rougher surface with larger particles. The rms roughness and *P–V* values of the Zn-doped SnO (annealed at 250 °C for 2 h) are 2.5 and 22.0 nm, and for SnO_2 (annealed at 500 °C for 10 h) are 75.0 and 587.4 nm, respectively. Growth of the particles during heat treatment is obviously observed and more noticeable in the case of the SnO_2 that is formed at higher temperature and longer time. Tetragonal shape of the SnO_2 also could be seen in Figs. 2(d) and 3(c).

The rms roughness of the undoped SnO and SnO_2 is 3.4 and 88.6 nm. *P–V* values of these films are 38.6 and 724.3 nm, respectively. It reveals that doping leads to finer and more uniform surface of the thin films.

The anodic performance of the Zn-doped SnO_2 thin film was investigated using galvanostatic charge/discharge in the potential range of 0–1.7 V (*vs.* Li/Li^+). Pure SnO_2 film was tested for comparison, too. The irreversible capacity of the Zn-doped nanocrystalline SnO_2 in the first cycle is 660.25 µAh cm^{-2} $µm^{-1}$. Therefore, Li^+ storage of the Zn-doped is higher than the pure SnO_2, as shown in Fig. 4(a). Initial coulombic efficiency of the Zn-doped SnO_2 is 57.78%, which is significantly higher than the pure SnO_2 (40.0%). Zn-doped SnO_2 with finer surface and smaller crystallite size would provides more reaction sites and reduces Li^+ diffusion length and improves initial efficiency. The plateau at around 0.9 V relates to the formation of the Li_2O and electrolyte decomposition due to the reaction of the SnO_2 with Li^+ corresponding to Eq. (2) [11]:

$$SnO_2 + 4Li^+ + 4e^- \rightarrow Sn + 2Li_2O \quad (2)$$

Li_2O formation and electrolyte decomposition during the first cycle caused a large irreversible capacity in SnO_2 electrodes. This reaction and subsequently electrolyte decomposition continued through next cycles, led to an increasing irreversible capacity and fading capacity of SnO_2. The other reduction and oxidation peaks at lower potentials (0.2 and 0.6 V) during the discharge are related to the formation of Li_xSn as mentioned in Eq. (3) [11]:

$$Sn + xLi^+ + xe^- \leftrightarrow Li_xSn \quad (3)$$

The cycling performances of the thin films are presented in Fig. 4(b). These data were obtained from constant charge/discharge at a current density of 10 µA cm^{-2} over the potential range 0–1.7 V. The reversible capacity of the thin films reduced with increasing the

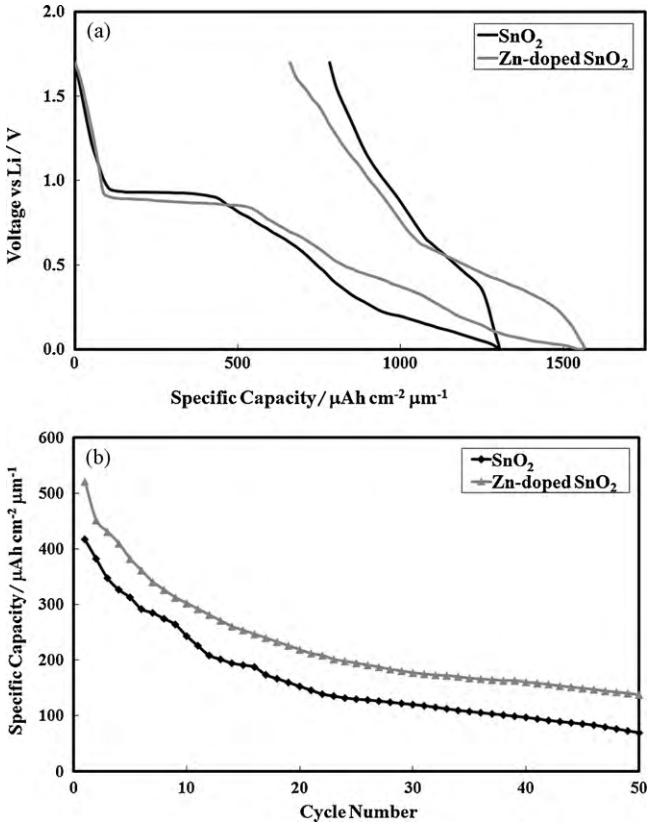

Fig. 4. (a) The first charge/discharge cycle between 0 V and 1.5 V and (b) the cyclic life of the nanocrystalline Zn-doped and pure tin oxide thin films ($i = 10\ \mu A\,cm^{-2}$).

cycle number. The reversible capacity of the pure and Zn-doped SnO_2 reached to 69.5 and 137.61 $\mu Ah\,cm^{-2}\,\mu m^{-1}$, respectively.

Increasing conductivity usually brings about more cyclability of doped materials. The n-type conductivity of the SnO_2 is due to the co-existence of oxygen vacancies (□) and interstitial tin atoms (Sn_i) [16]. Therefore, the n-type conduction could be driven with the following formula:

$$SnO_2 \leftrightarrow Sn^{4+}Sn_{ix}{}^{4+}O_{2-\varepsilon}@_{\varepsilon}[(2\varepsilon + 4x)e_{C.B.}{}^{-}] + \frac{\varepsilon}{2}O_2 \quad (4)$$

where $e_{C.B.}{}^{-}$ is the free electrons in the conduction band.

In our case, the electrical resistivity of the SnO_2 and Zn-doped SnO_2 were 1.050 and 1.072 kΩ cm, respectively. On the other hand, doping SnO_2 with substitutional cations with lower oxidation states than Sn^{4+} increases considerably the ceramic density [17]. Therefore, Sn^{4+} was substituted with Zn^{2+} and uncharged oxygen vacancies were formed according to following composition [18]:

$$Sn_{1-y}{}^{4+}Zn_y{}^{2+}O_{2-y}{}^{2-}@_y \quad (5)$$

The presence of oxygen vacancies leads to better mass transport at grain boundaries and increases density. If Zn^{2+} (0.74 Å) [19] is located in interstitial position, n-type conductivity will be possible according to:

$$Sn^{4+}Zn_x{}^{2+}O_2{}^{2-}[2xe_{C.B.}{}^{-}] \quad (6)$$

But, this phenomenon can be neglected due to the value of the resistivity of the undoped SnO_2 and Zn-doped SnO_2. Therefore, increasing conductivity is not the cause of the better cycling performance of the Zn-doped SnO_2.

Doping of SnO_2 with zinc atoms does not affect the tetragonal structure of the SnO_2 and only distorts the unit cell and reduces crystallite size of the SnO_2. In the following cycles, aggregation of the Sn particles to larger clusters in the Zn-doped SnO_2 occurred

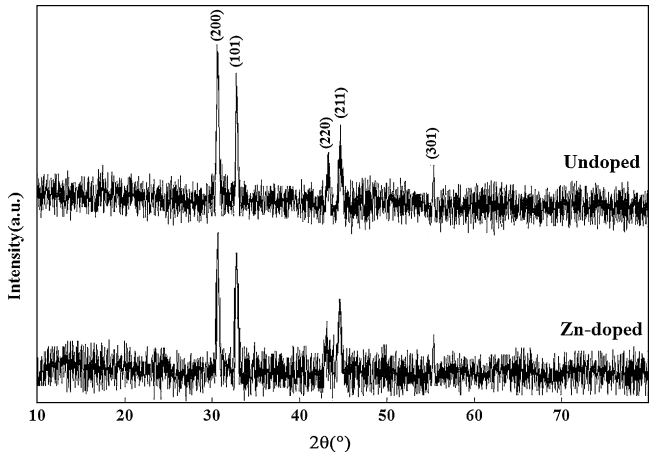

Fig. 5. X-ray diffraction of undoped and Zn-doped SnO_2 thin films after first and fifth cycles.

slower than undoped SnO_2. When a large Sn cluster formed, it is very appropriate to grow with gathering small Sn clusters. Consequently, the larger Sn cluster assembles smaller ones to minimize the surface energy among the particles [20]. The cohesion contact of the Sn clusters was collapsed for these large Sn particles due to the large volume change during cycling, results in poor capacity retention. X-ray diffraction patterns of the cycled undoped and Zn-doped SnO_2 are presented in Fig. 5. Clustering the Sn particles was done with a lower rate as could be seen in Fig. 5(b) for Zn-doped SnO_2. The crystallite sizes of the Sn are 187 nm and 138 nm for undoped and Zn-doped SnO_2, respectively.

4. Conclusions

Tin oxides thin films were deposited onto the glassy substrates using e-beam evaporation. As-deposited samples were consisted of amorphous SnO. Heat treatment at 250 °C for 2 h led to the crystallization of the SnO and subsequent treating at 500 °C for 10 h led to formation of the crystallized SnO_2. XRD showed that Zn-doped tin oxides had smaller crystallite size and a leftward shift of the spectrum. SEM images displayed a uniform and smooth surface of the thin films with homogeneous distribution of the Zn. The morphology of the SnO_2 was significantly different in respect of the other samples and consisted of larger particles. AFM images showed tetragonal morphology and rough surface of the SnO_2 thin films. However, surface morphology of the doped films was finer and more uniform with respect to the undoped films that increased initial coulombic efficiency of the Zn-doped snO_2. Also, reversible capacity of the Zn-doped SnO_2 was twice than the pure SnO_2 at fiftieth cycle. Finally, it was observed that doping of the SnO_2 prevented Sn clustering in addition to reducing particle sizes and improved cycling performance of the Zn-doped tin oxides.

References

[1] N.J. Dudney, J.B. Bates, R.A. Zuhr, S. Young, J.D. Robertson, H.P. Jun, S.A. Hackney, J. Electrochem. Soc. 146 (1999) 2455–2464.
[2] J.B. Bates, N.J. Dudney, D.C. Lubben, G.R. Gruzalski, B.S. Kwak, X. Yu, R.A. Zuhr, J. Power Sources 54 (1995) 58–62.
[3] Y.-L. Kim, H.-Y. Lee, S.-W. Jang, S.-J. Lee, H.-K. Baik, Y.-S. Yoon, Y.-S. Park, S.-M. Lee, Solid State Ionics 160 (2003) 235–240.
[4] D.G. Kim, H. Kim, H.-J. Sohn, T. Kang, J. Power Sources 104 (2002) 221–225.
[5] L.Y. Beaulieu, K.C. Hewitt, R.L. Turner, A. Bonakdarpour, A.A. Abdo, L. Christensen, K.W. Eberman, L.J. Krause, J.R. Dahn, J. Electrochem. Soc. 150 (2003) A149–151.
[6] Y.-L. Kim, S.-J. Lee, H.-K. Baik, S.-M. Lee, J. Power Sources 119 (2003) 106–109.
[7] N.C. Li, C.R. Martin, B. Scrosati, Electrochem. Solid-State Lett. 3 (2000) 316–318.
[8] Y. Idota, T. Kubota, A. Matsufuji, Y. Maekawa, T. Miyasaka, Science 276 (1997) 1395–1397.

[9] J.O. Besenhard, J. Yang, M. Winter, J. Power Sources 68 (1997) 87–90.
[10] I.A. Courtney, J.R. Dahn, J. Electrochem. Soc. 144 (1997) 2045–2052.
[11] N. Li, C.R. Martin, J. Electrochem. Soc. 148 (2001) A164–170.
[12] J. Fan, T. Wang, C. Yu, B. Tu, Z. Jiang, D. Zhao, Adv. Mater. 16 (2004) 1432–1436.
[13] S. Han, B. Jang, T. Kim, S.M. Oh, T. Hyeon, Adv. Funct. Mater. 15 (2005) 1845–1850.
[14] S. Panero, B. Scrosati, M. Wachtler, F. Croce, J. Power Sources 129 (2004) 90–95.
[15] B.D. Cullity, Elements of X-Ray Diffraction, 2nd ed., Addison-Wesley, London, 1978.
[16] C. Kilic, A. Zunger, Phys. Rev. Lett. 88 (2002) 095501.
[17] J. Fayat, M.S. Castro, J. Eur. Ceram. Soc. 23 (2003) 1585–1591.
[18] I. Saadeddin, H.S. Hilal, B. Pecquenard, J. Marcus, A. Mansouri, C. Labrugerea, M.A. Subramanian, G. Campet, Solid State Sci. 8 (2006) 7–13.
[19] R.D. Shannon, Cryst. Acta A 32 (1976) 751–767.
[20] Ch. Kim, M. Noh, M. Choi, J. Cho, B. Park, Chem. Mater. 17 (2005) 3297–3301.